Bioactive Materials 20 (2023) 355–367

Contents lists available at ScienceDirect

Bioactive Materials

journal homepage: www.keaipublishing.com/en/journals/bioactive-materials

Gold@Halloysite nanotubes-chitin composite hydrogel with antibacterial and hemostatic activity for wound healing

Puxiang Zhao [a,b], Yue Feng [a,b], Youquan Zhou [a,b], Cuiying Tan [a,b], Mingxian Liu [a,b,*]

[a] Department of Materials Science and Engineering, Jinan University, Guangzhou, 510632, China
[b] Engineering Research Center of Artificial Organs and Materials, Ministry of Education, Guangzhou, 510632, China

ARTICLE INFO

Keywords:
Nanotube
Chitin
Wound healing
Antibacterial
Photothermal hydrogel

ABSTRACT

Infection and healing of wounds after injury has always been an unavoidable problem in daily life, so design of a biomaterial with antibacterial and good wound healing properties is highly needed. Herein, a wound healing hydrogel dressing with halloysite clay and chitin as the main components was prepared, which combines the advantages of the biomacromolecule and clay. Halloysite nanotubes (HNTs) are extremely biocompatible clay materials with a hollow tubular structure, and the inner and outer surfaces of HNTs are composed of SiOx and AlOx layers with different charges. Au nanoparticles with diameter in 5–10 nm were filled into the HNTs' lumen to endow photothermal effect of the clay materials. Au@HNTs was then mixed with chitin solution to prepare flexible composite hydrogel by crosslinking by epichlorohydrin. The antibacterial properties, biocompatibility and hemostatic properties of the hydrogel material were investigated by antibacterial experiments, cell experiments, mouse liver and tail hemostatic experiments. After infecting the back wound of mice with Staphylococcus aureus, the hydrogel was applied to the wound to further verify the killing effect on bacteria and wound healing effect of the hydrogel material in vivo. The Au@HNTs-chitin composite hydrogel exhibits high antibacterial and hemostatic activity as well as promoting wound healing function with low cytotoxicity. This study is significant for the development of high-performance wound dressings based on two commonly used biocompatible materials, which shows promising application in wound sterilization and healing.

1. Introduction

Trauma is an extremely common clinical disease caused by cut, burns, scald, and diabetes, which greatly affects people's health and life quality. Severe trauma can cause major problems in the clinical healthcare [1,2]. Bleeding and infection are inevitable issue in the wound care, which can lead to shock, disability and even death [3]. Wound infection occurs when germs, such as bacteria, grow within the damaged skin of a wound, which can bring pain, swelling, and redness of the wound area [4,5]. In order to ensure rapid and healthy wound healing, wound hemostasis and post-injury treatment by dressing made from biomaterials are particularly important. For a long time, the development of multifunctional and high-performance hemostatic materials to treat wound bleeding and infection is imminent.

Studies have shown that many silicate minerals have good hemostatic effect [6], such as zeolite, montmorillonite, kaolin, etc. They are low-cost and have good biocompatibility [7], and immune rejection rarely occurs. Among them, halloysite clay nanotubes (HNTs) represent a high-performance homeostat and wound healing materials. HNTs have a molecular formula of $Al_2Si_2O_5(OH)_4{\cdot}nH_2O$, which are natural and environmentally friendly silicate clay mineral [8,9]. Previous studies have shown that HNTs have a superior hemostatic effect when comparing with other clays such as montmorillonite and kaolin [10]. Interestingly, HNTs are tubular nanoparticles with an empty lumen, and the typical size of HNTs includes length of 200 nm–1 μm, outer diameter of 50–70 nm, and inner diameter of 10–30 nm [11,12]. The lumen of HNTs have a strong loading capacity and can be filled with different particles or drug molecules [13,14]. Metal particles can be loaded in the tube to achieve photothermal performance [15,16], thereby achieving the effect of photothermal sterilization. This not only has the effect of caring for the wound to avoid infection, but also the temperature rising can provide a warm environment that is conducive to wound repair and accelerate wound healing [17,18]. However, as a clay powder, HNTs are difficult to handle in practical applications for wound care. So, HNTs

Peer review under responsibility of KeAi Communications Co., Ltd.
* Corresponding author. Department of Materials Science and Engineering, Jinan University, Guangzhou, 510632, China.
E-mail address: liumx@jnu.edu.cn (M. Liu).

https://doi.org/10.1016/j.bioactmat.2022.05.035
Received 14 April 2022; Received in revised form 23 May 2022; Accepted 30 May 2022

were usually mixed with polymer matrix or coated on polymer fiber surface to prepare composite dressing [19]. As a wound dressing, hydrogel materials have many advantages, which can not only seal the wound blood vessels to achieve the purpose of hemostasis [20,21] but also provide a moist environment to prevent infection and accelerate wound healing [22,23]. In addition, the hydrogel has certain toughness, softness and flexibility, which enables the hydrogel better covering on wounds in different parts. HNTs powder can be combined with different polymer solution to form composite hydrogel with synergistic effect of both substances, and it will be of great help in clinical treatment.

In this study, Au@HNTs were prepared by filling the lumen of HNTs with Au nanoparticles with uniform sizes by in-situ growth method. The Au@HNTs not only has excellent photothermal properties, but also has good application in the field of catalysis. Hydrogel network was then constructed with chitin as a matrix for incorporation Au@HNTs, forming an Au@HNTs-chitin hydrogel with photothermal effect. Chitin is selected as the hydrogel matrix, because it comes from renewable natural resource with hemostatic and antibacterial properties [24]. It mainly exists in the exoskeleton structure of shrimps and crabs [25,26], and has good biocompatibility and processability. The Au@HNTs-chitin hydrogel not only has good hemostatic ability and photothermal antibacterial ability, but also retains the advantages of hydrogel material. They can be cut and bent, which can achieve hemostasis and antibacterial effects in different parts and types of wounds. The high-performance dressings based on modified HNTs and chitin shows promising application in wound sterilization and healing.

2. Results and discussion

2.1. The preparation process and application of Au@HNTs-chitin hydrogel

The preparation process and application of Au@HNTs-chitin hydrogel are shown in Fig. 1. Filling of Au nanoparticles (NPs) with controlled sizes into the lumen of HNTs using the Wiley's method [27]. Toluene and ethanol mixed solution (in a ratio of 1:1) were selected as the reaction medium, then a small amount of oleic acid (OAc) and oleylamine (OAm) were added as a surfactant for the Au NPs synthesis. HNTs and $HAuCl_4$ were added in the afore-mentioned solution as the reactant. Under the action of capillary force, Au^{3+} and OAc, OAm molecules were loaded into the HNTs tube, and ascorbic acid was used as reducing agent. Au^{3+} were reduced to Au NPs in the interior of HNTs to form Au@HNTs. In this process, Au NPs are not only reduced in the tube, but also form Au NPs outside the tube (Fig. S1). To remove free Au

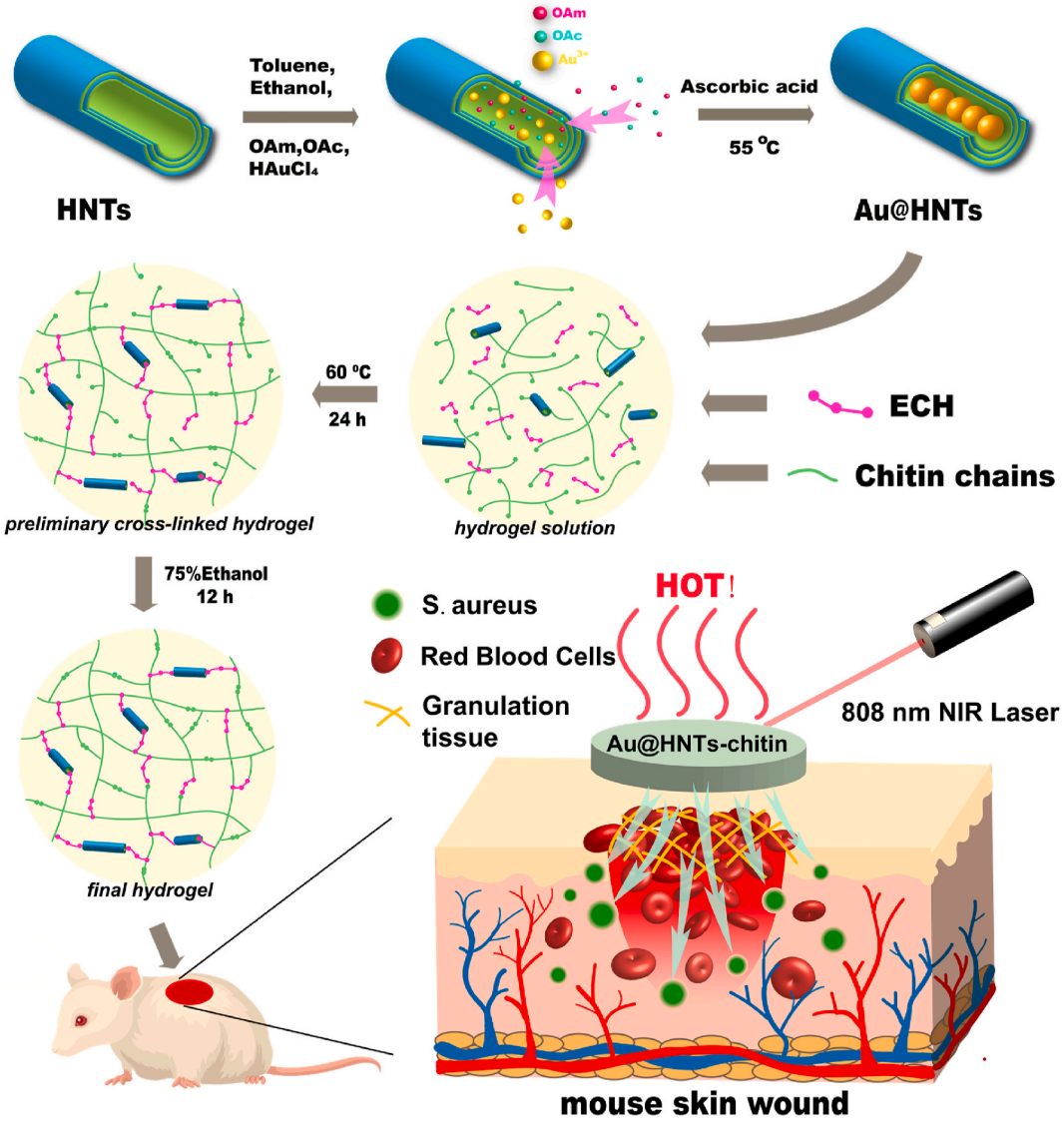

Fig. 1. Schematic showing the preparation process and application of Au@HNTs-chitin hydrogel.

NPs outside the tube, Au@HNTs were washed by centrifugation using toluene as a solvent. The chitin solution and Au@HNTs powder were then stirred and mixed, and epichlorohydrin (ECH) was added as a cross-linking agent. ECH is an efficient cross-linking agent for chitin and HNTs, it can form a covalent ether bridge between the OH group of the chitin chain and the hydroxyl groups on the HNTs. The covalent bonds between chitin and HNTs are responsible for the formation and enhanced properties of hydrogel materials. Soaking in ethanol will further improve the mechanical properties since the gel network shrink to dense structure. Finally, the Au@HNTs-chitin hydrogel with anti-bacterial and hemostatic activity was applied in wound healing.

2.2. Characterization of Au@HNTs

TEM images of HNTs and Au@HNTs are shown in Fig. 2A and B, respectively. It can be seen that the lumen of HNTs is transparent and empty. While the lumen of Au@HNTs is filled with small black round particles, most of the particles ranges from 5 to 10 nm in diameter. To confirm the composition of these small particles, TEM analysis of Si, Al, and Au elemental mapping was performed on the Au@HNTs (Fig. 2C), and the results are shown in Fig. 2D. Obviously, Al and Si elements exist inside and outside the Au@HNTs, while Au elements only exist in the interior of the tube. This suggests that the Au NPs successfully entered the cavity of the HNTs.

The FTIR results of the HNTs before and after Au NPs loading were shown in Fig. 2E. As a metal element, there was no vibrational peak in the infrared spectrum of Au NPs, so the spectrum of Au@HNTs was consistent with that of HNTs. This proves that the process did not change the chemical composition and microstructure of HNTs. XRD results in Fig. 2F show that there are Au-specific (111), (200) and (220) crystal planes on the pattern of Au@HNTs, and HNTs retained the original peaks. Fig. 2G shows the UV–vis absorption spectra of Au NPs, HNTs and Au@HNTs. Au NPs have a characteristic absorption at 530 nm, and Au@HNTs have the same absorption band in this region.

Fig. 2H and I are the XPS spectra of Al and Au elements of HNTs and Au@HNTs, respectively. It can be seen that a large amount of Au NPs exists in Au@HNTs. In addition, the survey of XPS spectra (Fig. S2) also proved this conclusion. Therefore, all the evidences indicated that Au

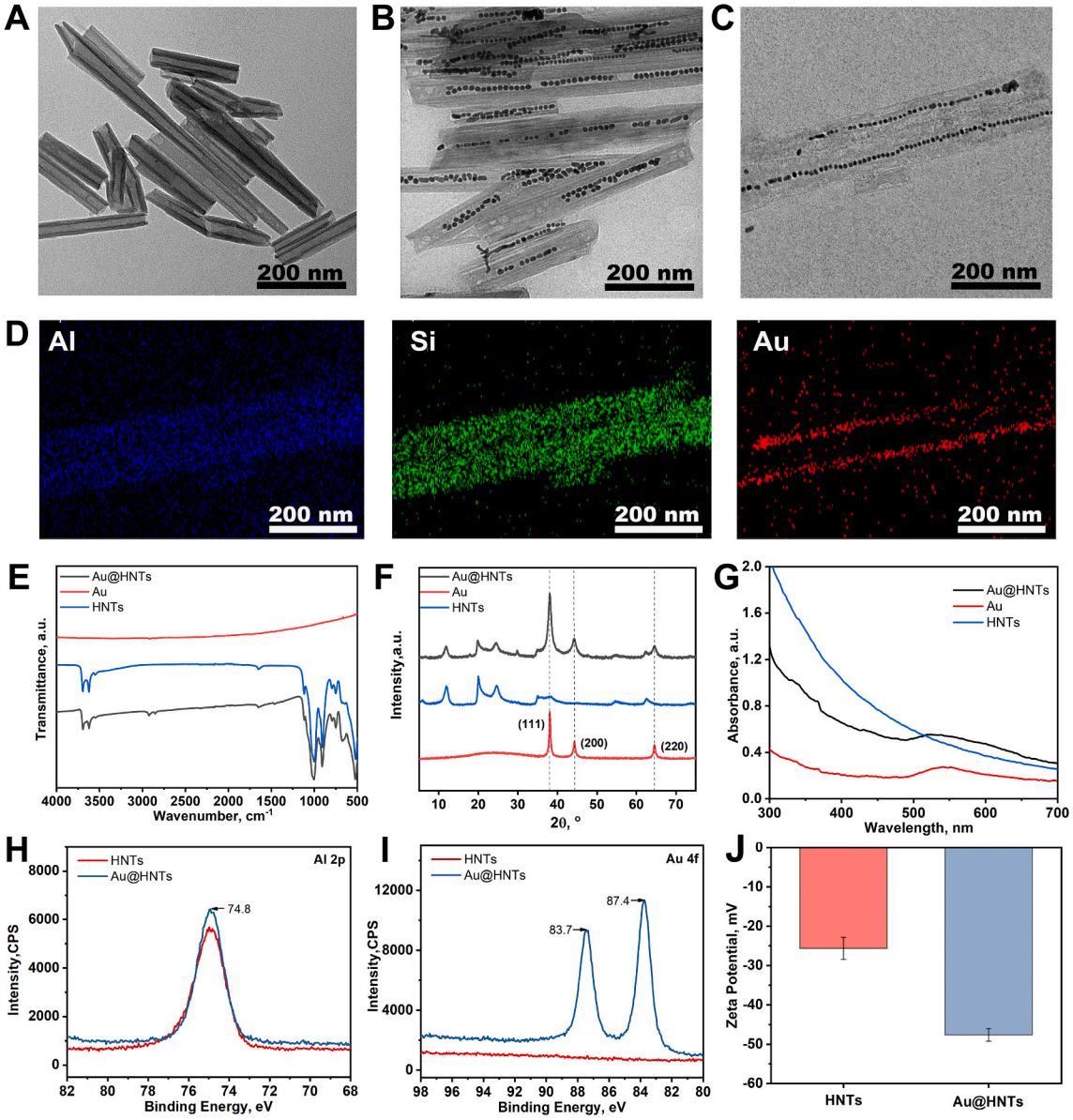

Fig. 2. TEM images of (A) HNTs and (B)(C) Au@HNTs. (D) Mapping images of Al, Si, and Au elements of Au@HNTs in (C). (E) FTIR spectra; (F) XRD patterns; (G) UV–vis absorption spectra of different samples.(H) (I) XPS and (J) zeta potential of HNTs and Au@HNTs.

NPs were formed in HNTs successfully. The zeta potential in Fig. 2J shows that HNTs are negatively charged because the negative charge outside the tube is greater than the positive charge inside the tube. While Au@HNTs showed significantly stronger negative charge. The reason is that the positive environment of the inner wall of Au@HNTs is covered due to the filling of Au NPs, resulting in a stronger negative charge than HNTs. This also suggests that Au NPs entered the tube of HNTs. In addition, particle size analysis on HNTs and Au@HNTs was performed (Fig. S3). It can be seen that the particle size difference between Au@HNTs and HNTs is small, and the particle size distribution is nearly the same. So, the process of preparing Au@HNTs did not damage the original HNTs and preserved the original morphology of HNTs. Nitrogen adsorption tests show that the adsorption capacity of Au@HNTs for nitrogen became weak, and the specific surface area (23.6 m^2/g) is about half of that of HNTs. The reason is that the tube of Au@HNTs is filled with Au NPs, which reduces the porosity, so the adsorption capacity of nitrogen is inferior to that of the original HNTs. The photothermal conversion efficiency of Au@HNTs was determined as 19.3% which is lower than that of Au NPs. This is also attributed to the shielding effect of HNTs lumen.

2.3. Catalytic activity of Au@HNTs

It is widely recognized that the catalytic activity of the catalyst depends on particle size, and the smaller particle show better catalytic effect [28]. Therefore, the agglomeration of catalyst particles affects the catalytic effect [29]. Au@HNTs have a unique core-shell structure, and the Au NPs have good dispersion state in the lumen of HNTs. The wall of HNTs restrict the growth of Au NPs and control their particle size, so the confinement effect of HNTs prevents the agglomeration of Au NPs. This makes Au@HNTs possess better catalysis performance. Nitrosophenol (4-NP) is one of the most common organic pollutants in industrial and agricultural wastewater [30], while 4-aminophenol (4-AP) has very important application value in analgesic and antipyretic drugs, imaging agents, corrosion inhibitors and other applications [31]. Reduction of 4-NP to 4-AP using noble metal nanomaterials as catalysts is the most commonly used method for treatment of 4-NP [32,33].

In this work, referring to Wen's method [34], the reduction of 4-NP by sodium borohydride was used as a model reaction to evaluate the catalytic performance of the as-prepared Au@HNTs. It was convenient for UV–Vis absorption spectroscopy to monitor the structure change of 4-NP. According to the standard curve of 4-NP in Fig. S5A, the UV absorption peaks after adding Au NPs and Au@HNTs are obtained in Figs. S5B and C, respectively. It can be observed that the absorption peak at 400 nm gradually decreased after the catalyst was added, but the absorption peak of the Au@HNTs group as catalyst decreased more obviously. The absorption peak disappeared after 5 min, and a new absorption peak appeared at 300 nm. This indicated that 4-NP was converted to 4-AP under the catalysis of Au@HNTs, and the conversion process was nearly completed at 6 min. Fig. S5D shows the appearance of the solution before and after conversion. The 4-NP solution is pale yellow, while the 4-AP solution is colorless. In contrast, the group with Au NPs as catalyst had lower catalytic efficiency, and no new absorption peak appeared at 300 nm at 6 min. Therefore, the experimental time were further extended to 25 min, and the obtained UV absorption peak changes are shown in Fig. S5E. It can be seen that the absorption peak at 400 nm decreases continuously, and the absorption peak at 300 nm appears. The conversion of 4-NPs with Au NPs and Au@HNTs as catalysts is shown in Fig. S5 G. This demonstrated that Au@HNTs also successfully catalyze the conversion of 4-NP to 4-AP, but the catalytic efficiency is much higher than that of Au NPs. The reason is that Au NPs in Au@HNTs have small particle size and do not agglomerate, so they have strong catalytic ability and can complete the catalytic reaction in a short time. After the reaction, the Au@HNTs were separated by centrifugation, washed with ethanol, and then reused for the next round under the same conditions. The catalytic activity of Au@HNTs did not decrease significantly after three consecutive cycles, and the experimental results are shown in Fig. S5H. It shows that the Au@HNTs catalyst has long-term stability and can be recycled.

2.4. Structure and properties of Au@HNTs-chitin

The synthesis of Au@HNTs-chitin composite hydrogel was illustrated in Fig. 1. Referring to the method of Liu [35], Au@HNTs-chitin with Au@HNTs contents of 2.5%, 5%, and 10% were prepared. The covalent bonds of chitin and HNTs with ECH and ethanol immersing induced physical crosslinking are two critical factors for the good mechanical properties of the hydrogel [36]. Fig. 3A is a photograph of the hydrogel at different stages during the preparation process. It can be seen both the solution and the hydrogel are uniform with black color. The hydrogel can be self-standing with satisfied mechanical properties. Fig. 3B compares the FTIR curve of different samples. For pure chitin, the stretching of C–H band is located at 2877 cm^{-1}, amide-I band in CONH group appeared at 1650 cm^{-1}, the C–O–C band in glucopyranose ring appears at 1160 cm^{-1}, and the C–O band at 1070 and 1030 cm^{-1} [37]. For Au@HNTs-chitin, the peak at 3695 cm^{-1} was attributed to the stretch to the internal surface hydroxyl group, and the peak around 3620 cm^{-1} was attributed to the internal hydroxy group [38]. The absorbance intensity of the hydrogel samples varied slightly at 1650 and 1630 cm^{-1} assigned to amide bands due to the hydrogen-bond interactions between chitin and Au@HNTs.

The XRD results of the samples were shown in Fig. 3C. It can be seen that there are Au diffraction peaks corresponding to (020) and (111) crystal planes in Au@HNTs-chitin, and these peaks become more obvious with the increase of Au@HNTs concentration. This shows that Au@HNTs are successfully embedded in the chitin matrix. The rheology results of the hydrogels are shown in Fig. 3D. Storage modulus (G′) and loss modulus (G″) of the composite hydrogels increase with the loading of Au@HNTs. The G′ and G″ of 10% Au@HNTs-chitin are 4.6×10^5 and 2.2×10^5 Pa, respectively, which are higher than those of pure chitin. This indicates that Au@HNTs-chitin has better strength and toughness, which is suitable for wound dressing applications. The increase in modulus is attributed to the reinforcing effect of the rigid tubular nanoparticles of HNTs to the soft polymer matrix. The compression stress-strain curve was shown in Fig. 3E. Similarly, the strength of the hydrogel increases by the incorporation of Au@HNTs. For example, the compressive stress at 80% deformation is 17.5, 34.4, 51.4, 64.1 kPa, for pure chitin, 2%, 5%, 10% hydrogel, respectively. This also demonstrate the reinforcing effect of the HNTs towards chitin hydrogel, which is beneficial for practical application in wound treatment.

SEM analysis were performed to character the microstructure of the hydrogel (Fig. 3F). At low magnification images, the pores of pure chitin are the largest, and the pores of the hydrogel after adding Au@HNTs become smaller. With the increase of Au@HNTs concentration, the pores of the hydrogel became smaller and smaller. The pores of 10% Au@HNTs-chitin were the smallest, and the pores number in the same area were the most. The presence of the tubular nanoparticles depresses the growth of ice crystal into large size, which leads to the decreased pore size [39]. Also, the surface of the pure chitin was smooth, and the pores wall in composite were rough due to the introduction of nanoparticles. At high magnification, it was found that Au@HNTs embedded in the inner of chitin and adhered to each other, which enhanced the strength of chitin matrix. As expect, there are more rod-like structures by the increase of Au@HNTs concentration. This explained that Au@HNTs can enhance the mechanical strength of the chitin hydrogels. Fig. S6 shows the element mapping images of C, N, O, Al and Si of Au@HNTs-chitin. It can be seen that O, Al, Si elements of HNTs are presence, which further proves that Au@HNTs are distributed inside the chitin hydrogel on micro size.

The effect of Au@HNTs-chitin hydrogel as a photothermal materials was then investigated. An infrared camera was used to record the temperature change of Au@HNTs-chitin under 808 nm infrared laser

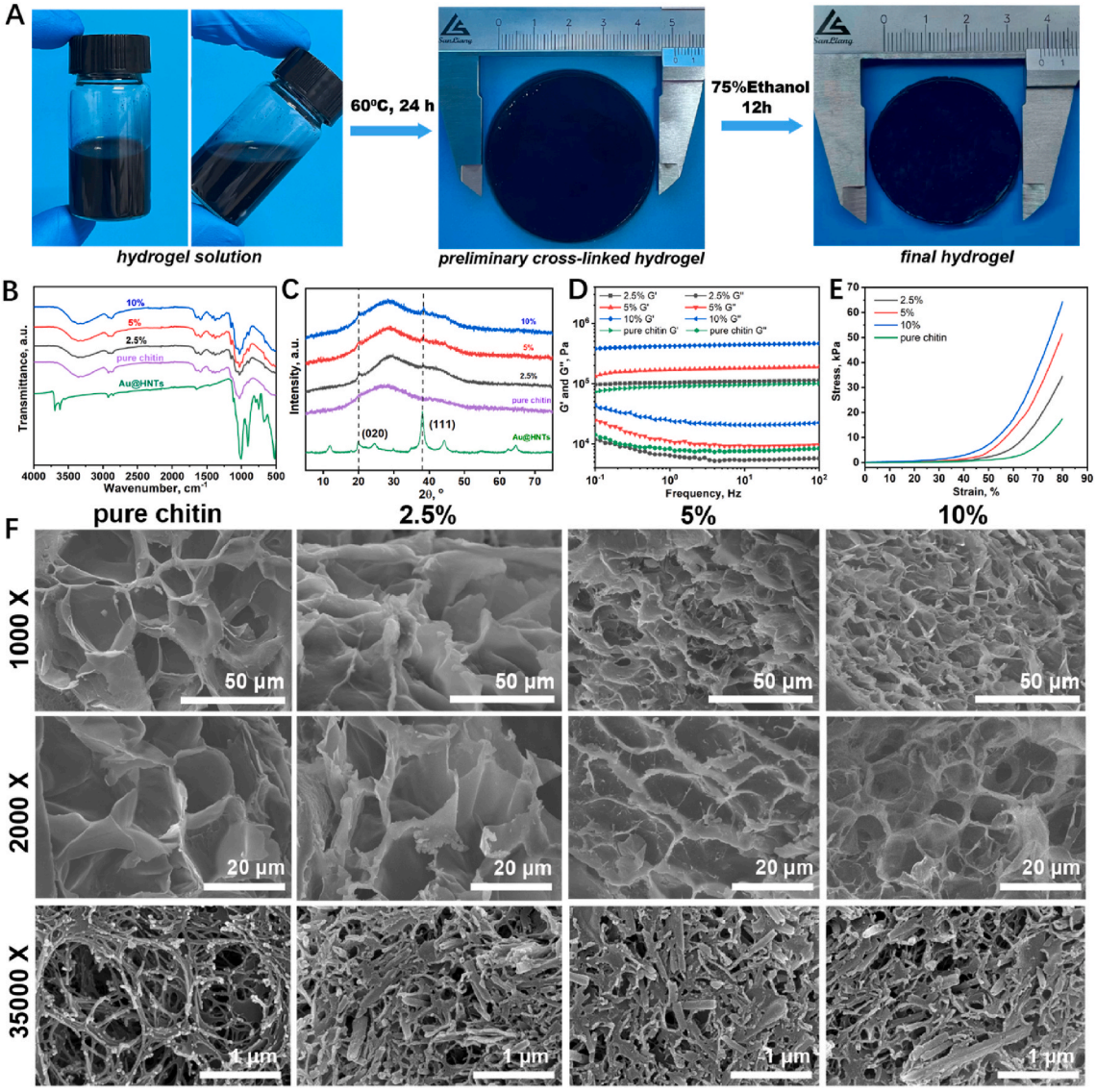

Fig. 3. (A) Photographs during the preparation of Au@HNTs-chitin. (B) FTIR spectra; (C) XRD patterns; (D) Rotational rheology curve; (E) Stress-strain curves of different hydrogel. (F) SEM images of Au@HNTs-chitin and pure chitin.

irradiation for 8 min. Taking pure chitin as the control group, different concentrations of Au@HNTs of 2.5%, 5% and 10% and different infrared powers of 0.8, 1.6 and 2.2 W/cm^2 were applied, respectively. Fig. 4A shows a graph of temperature changes for different groups under different conditions. Fig. 4B and C shows the temperature change curves of hydrogels with different compositions under the irradiation of 2.2 W/cm^2 infrared light and the temperature change curves of 10% Au@HNTs-chitin under the irradiation of different powers of infrared light, respectively. It can be seen that pure chitin and HNTs-chitin have no photothermal effect, while Au@HNTs-chitin has a good photothermal effect. Under the same power of infrared light irradiation, the higher the content of Au@HNTs, the better the photothermal effect. Similarly, when the content of Au@HNTs remains unchanged, the higher the power of infrared light, the better the photothermal effect. Under the irradiation of 2.2 W/cm^2 infrared light, the temperature of 10% Au@HNTs-chitin can be increased by about 40 °C, which is enough to kill various bacteria and malignant tumors. The photothermal effect of Au@HNTs-chitin can be reproduced multiple times when the infrared light is turned on or off, as shown in Fig. 4D. This indicates that the photothermal effect of Au@HNTs-chitin is stable and reproducible during photothermal therapy. In addition, the thermal images before and upon the laser irradiation of the hydrogel were taken, which was shown in Fig. S7. It can be seen that the heat inside the hydrogel diffuses rapidly to various parts due to the thin hydrogel sample after turning on infrared laser. The heat can quickly kill the bacterial in the wound area without harm to healthy tissue. Since Au@HNTs has an absorption peak around 550 nm (Fig. 2G), a green laser can not bring photothermal effect of the hydrogel.

2.5. Cytotoxicity assay

As a wound hemostasis and healing dressing, the biosafety of Au@HNTs-chitin is crucial. Based on previous studies on skin safety, the mouse fibroblast cell line L929 were selected as an in vitro model [40, 41]. The cytotoxicity was assessed by exposing L929 mouse fibroblasts in PBS (control group) and different concentrations of Au@HNTs-chitin leaching solution for 24 and 48 h. After treatment, cell viability was detected using Cell Counting Kit-8 (CCK-8) method. The results are shown in Fig. 5A and B. The survival rate of cells in all concentrations of Au@HNTs-chitin groups was over 80% at 24 h, and even over 90% in most groups. At 48 h, except for the 30 mg/mL 10% Au@HNTs-chitin group, the cell viability of other groups is higher than 80%. This

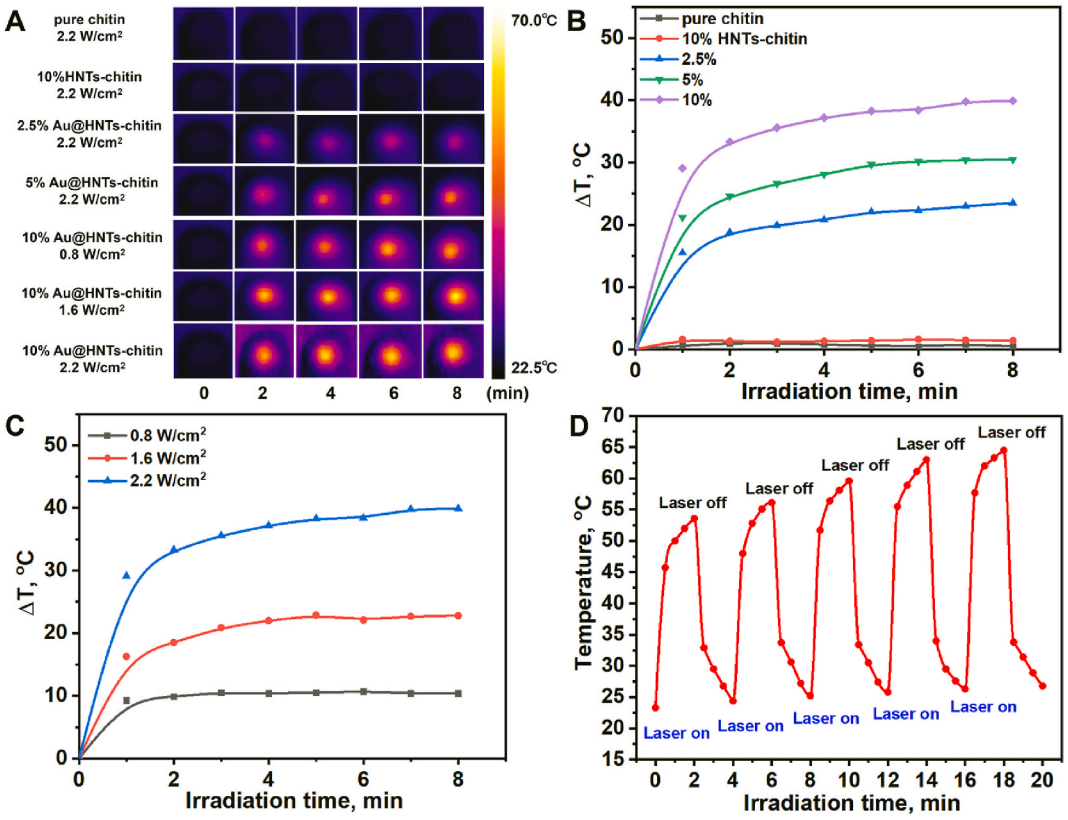

Fig. 4. (A) Thermal images of Au@HNTs-chitin at different concentrations and different powers under irradiation of 808 nm by infrared camera; (B) Temperature curves of pure chitin, HNTs-chitin and Au@HNTs-chitin with different concentrations irradiated by an 808 nm laser (2.2 W/cm^2); (C) Temperature curves of 10% Au@HNTs-chitin upon 808 nm laser irradiation with various powers; (D) Temperature change of Au@HNTs-chitin with an 808 nm laser switch-on/off five times.

indicates that Au@HNTs-chitin has little toxicity to cells, while Au@HNTs-chitin with lower Au@HNTs content has almost no toxicity to cells.

For further observation of cell survival, the dual acridine orange/ethidium bromide (AO/EB) staining was used to differentiate live/dead cells. AO can penetrate normal cells with intact cell membranes and early apoptotic cells, and show green fluorescence after binding to DNA. At the same time, EBs stained late apoptotic and necrotic cells, emitting orange-red fluorescence when bound to nuclear DNA. The different groups of Au@HNTs-chitin at 15 mg/mL were subjected to live and dead staining (Fig. 5C). The experimental results exhibit green color cells at 24 h or 48 h, except for the negligible orange-red fluorescence in the 10% Au@HNTs-chitin treated group.

Subsequently, the cells were treated with 15 mg/mL Au@HNTs-chitin leaching solution, and the growth state of cells was assessed by flow cytometry (Fig. 5D). The AnnexinV-FITC-negative/PI-negative cells in the lower left quadrant are normal cells, and the other three quadrants represent early, mid-stage apoptotic and necrotic cells, respectively. The proportions of the corresponding cell populations were labeled in the upper right corner of each quadrant. The results show that the proportion of cell population in the Au@HNTs-chitin group remained above 90% regardless of the concentration, which was not significantly different with the control group. About 5% of spontaneously apoptotic cells were considered normal due to inevitable fluctuations in spontaneously apoptotic cell status and irritation caused by sample preparation. It can be seen that the results of flow cytometry also confirmed that Au@HNTs-chitin has good cytocompatibility.

2.6. In vitro antibacterial performance

The potential antibacterial properties of Au@HNTs-chitin were investigated using *Escherichia coli* (*E. coli*) and *Staphylococcus aureus* (*S. aureus*) as experimental models. The group without any treatment was used as the blank control group, and pure chitin, HNTs-chitin and Au@HNTs-chitin with different Au@HNTs contents were used as the experimental group. After mixing with the bacterial suspension, it was irradiated under an infrared laser with a power of 1.6 W/cm^2 for 5 min, and then coated on an agar plate, and the result after incubation for 12 h is shown in Fig. 6A. The number of colonies on the agar plate was counted, and the results of *E. coli* and *S. aureus* were shown in Fig. 6B and C, respectively. It can be observed that Au@HNTs-chitin has antibacterial effect on both bacteria. For *E. coli*, the antibacterial effect was enhanced with the increase of Au@HNTs content. The 2.5% Au@HNTs-chitin agar plate had relatively few colonies, while the 5% Au@HNTs-chitin agar plate had a few colonies, and the 10% Au@HNTs-chitin agar plate had no colonies at all. This suggests that the heat generated by the weak photothermal effect is not enough to inhibit the reproduction of *E. coli*, and a higher temperature is required. For *S. aureus*, the antibacterial effect of Au@HNTs-chitin is more obvious, and no colonies are formed on the agar plates for the 2.5%, 5% and 10% groups. This indicates that the photothermal effect of Au@HNTs-chitin can kill bacteria under the irradiation of infrared laser with a proper power.

2.7. In vivo hemostatic performance

In order to determine the hemostatic properties of Au@HNTs-chitin, two models of hemostasis in mouse liver and mouse tail were employed [42], as shown in Fig. 7A. For the mouse tail hemostasis experiments, photographs of the four time periods are shown in Fig. 7B. It can be clearly seen that the blood volume of the materials group in the treatment of tail wound is significantly less than that of the control group, while the hemostatic effect of HNTs-chitin and Au@HNTs-chitin is better than that of pure chitin. The hemostasis time and the amount of blood loss for each group are shown in Fig. 7C. Pure chitin, HNTs-chitin

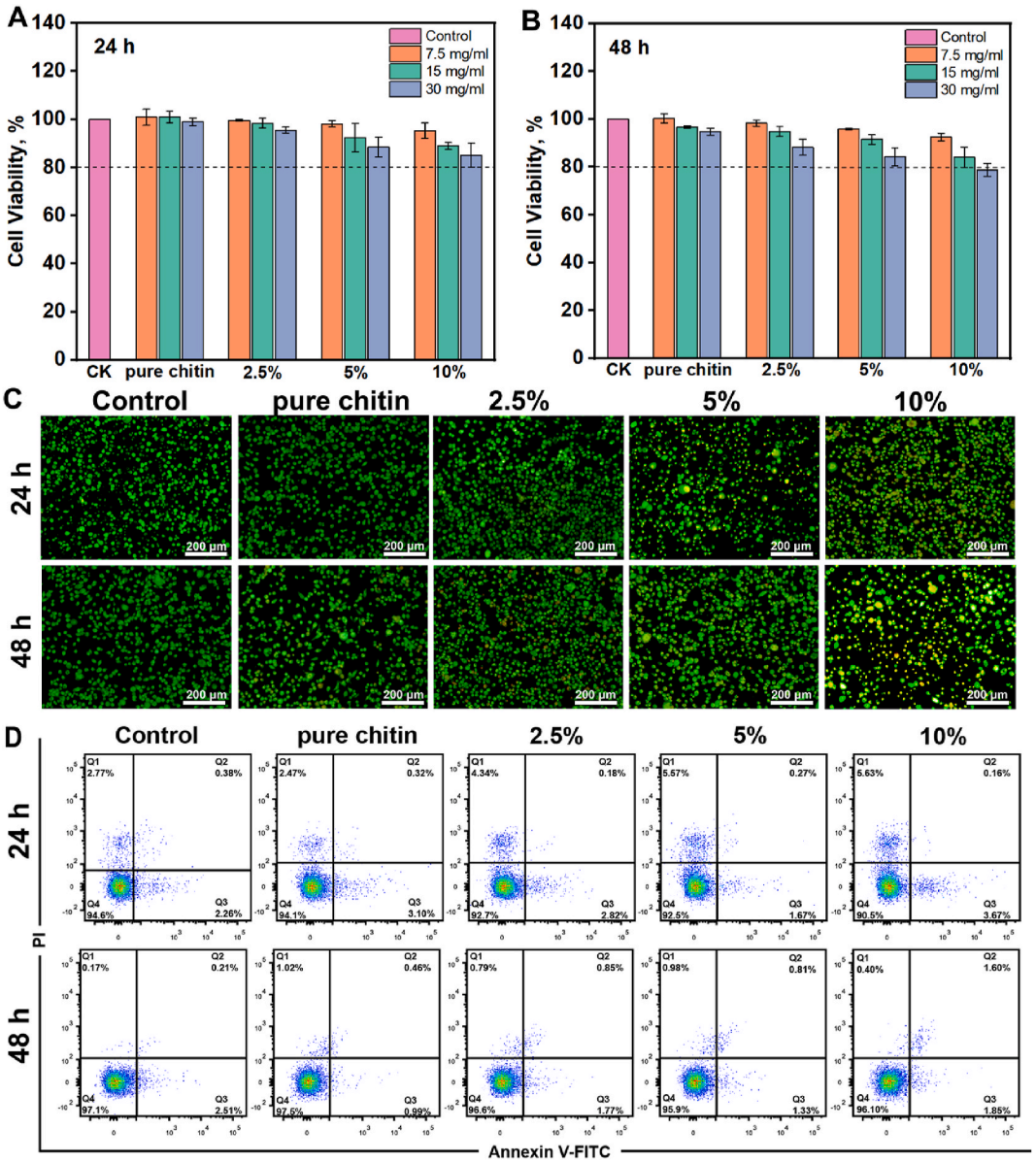

Fig. 5. (A)(B) Cytotoxicity of Au@HNTs-chitin in vitro by the CCK-8 method. (C) AO/EB live/dead staining images of mouse fibroblasts (L-929) cultured for 24 and 48 h. (D) Apoptosis and necrosis results of L-929 cultured with Au@HNTs-chitin for 24 and 48 h by the flow cytometry method.

and Au@HNTs-chitin can control the hemostasis time within 6 min, but the blood loss of pure chitin group is more than the other two experimental groups. Therefore, HNTs-chitin and Au@HNTs-chitin has better hemostatic effect.

For the liver hemostasis model, a pre-weighed filter paper was placed under the liver to support the bleeding volume of the liver wound. The final wound bleeding photo is shown in Fig. 7D. It can be seen that blood loss was relatively less in HNTs-chitin group and Au@HNTs-chitin group. The results of Fig. 7E were obtained by counting the hemostasis time and blood loss. It can be seen that the hemostasis time of all experimental groups was significantly reduced, especially the HNTs-chitin group and the Au@HNTs-chitin group. In terms of blood loss, the Au@HNTs-chitin group was the least, followed by the HNTs-chitin group. These experimental results fully demonstrate the hemostatic effect of Au@HNTs-chitin and HNTs-chitin. HNTs show high hemostatic properties, since they can make the blood in the wound form blood clots, trigger the intrinsic coagulation cascade, and accelerate the formation of platelets to achieve hemostasis [10]. Therefore, whether it is HNTs-chitin or Au@HNTs-chitin, HNTs not only play a certain role in the strength of the material, but also endow the material with good hemostatic ability.

2.8. *In vivo* wound healing efficacy

In order to study the antibacterial effect and wound healing ability of Au@HNTs-chitin in vivo, a mouse wound infection model was made and treated [43]. A schematic diagram of the entire process is shown in Fig. 8A. After creating circular wounds on the backs of mice by scissors, the wounds were infected with Staphylococcus aureus. Subsequently, the hydrogel is covered on the wound surface, and infrared light are irradiated to achieve the sterilization effect. In order to ensure that the damage to the normal cells is minimized, the temperature of the hydrogel is controlled at around 45 °C, as shown in Fig. S8. During this process, the mechanical properties and flexibility of the hydrogel almost did not change. Fig. 8B is a photo of wounds infected for different days in different experimental groups and a photo of colonies of *S. aureus* at the infected site after 12 h of incubation on agar plates. The wounds without bacteria was used as the control group, and the wound without any

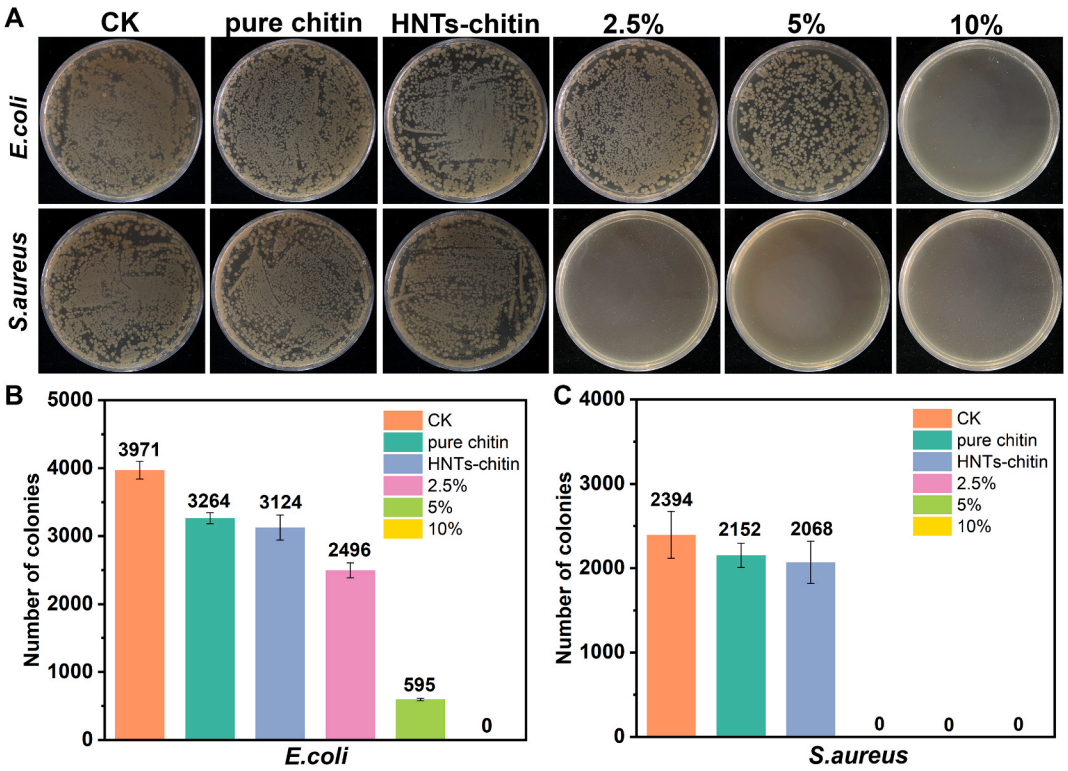

Fig. 6. (A) Growth of *E. coli* and *S. aureus* cultured in vitro on agar plates under different conditions. Number of colonies of *E. coli* (B) and *S. aureus* (C) on agar plates.

treatment after infection with bacteria was used as the model group.

Fig. 8C shows the comparison of wound area analyzed with ImageJ software. It can be seen that the wounds in the model group healed very slowly, and 40% of the wound area still existed until the 7th day. The Au@HNTs-chitin group had an obvious wound healing effect, and the healing speed was comparable to that of the control group, and only 20% of the wound area remained on the 7th day. Furthermore, the number of colonies on the agar plate of the Au@HNTs-chitin group was significantly less than that of the other groups. In order to prove the antibacterial effect of Au@HNTs-chitin on the infected wound, the OD value of the tissue fluid at the infected site was measured and the number of colonies on the agar plate was counted. The OD value and the number of colonies are shown in Fig. 8D and E. It can be seen that the OD value of the Au@HNTs-chitin group was significantly lower than that of other experimental groups, and the number of colonies was far less than that of other experimental groups. This indicates that Au@HNTs-chitin can effectively kill and inhibit bacterial growth at the wound infection site, thereby reducing wound infection and promoting healing quickly. Since both the Au NPs and HNTs are not degradable in vivo, so the prepared hydrogel acts as temporary dressing materials for wound healing. After treatment of the wound, the hydrogels are gently moved from the wound.

Collagen deposition is a key factor in determining skin strength and appearance [44], so wound tissue on day 7 was taken for Masson staining (Fig. 8F). It can be seen from the intensity and area of blue staining that there are significant differences in collagen deposition between the experimental groups. Among them, the Au@HNTs-chitin group has the highest collagen deposition density, which is similar to the control group. This shows that the wound healing effect of the Au@HNTs-chitin group is the best in the present experiment. Meanwhile, blood routine tests were performed on mice in different groups, as shown in Fig. S9, and the blood components of mice in different groups did not change much. And the body weight changes of the mice were recorded, as shown in Fig. S10. It can be seen that the weight of mice in the Au@HNTs-chitin group maintained an upward trend, which was consistent with the control group. These demonstrate the high antibacterial ability of Au@HNTs-chitin and the satisfied effect of promoting wound healing.

The main materials of the prepared composite hydrogel, chitin and halloysite, are natural, inexpensive and highly biocompatible. Moreover, most of the commercial wound healing dressing materials, such as gelatin, hyaluronic acid, and alginic acid hydrogels, have poor hemostatic function. The addition of porous and negatively-charged HNTs endows the hydrogel with superior hemostatic properties [10,19]. Clinical treatment of wound by this hydrogel materials is based on photothermal of Au NPs loaded in HNTs lumen and soft chitin hydrogel matrix, rather than using anti-inflammatory drugs, which reduces the risk of allergic reactions in patients. In practical application, a treatment period can be completed in only a few minutes, so the efficiency is high, which also can reduce the patient complaints.

3. Conclusions

Au NPs were filled into the lumen of HNTs to synthesize Au@HNTs with photothermal effect. A chitin hydrogel was further employed to load Au@HNTs, and a hemostatic antibacterial hydrogel with proper mechanical properties and tailorable photothermal effect was obtained. The cytotoxicity test shows the high cytocompatibility of Au@HNTs-chitin hydrogel. In vitro antibacterial experiments suggest the photothermal antibacterial ability towards *E. coli* and *S. aureus*, while the hydrogel show high hemostatic performance in mouse liver and tail bleeding. Wound infection healing results confirmed the in vivo antibacterial and healing-promoting effect of the hydrogel material. This study developed a multifunctional medical hydrogel integrating antibacterial and hemostasis based on chitin and metal filled HNTs.

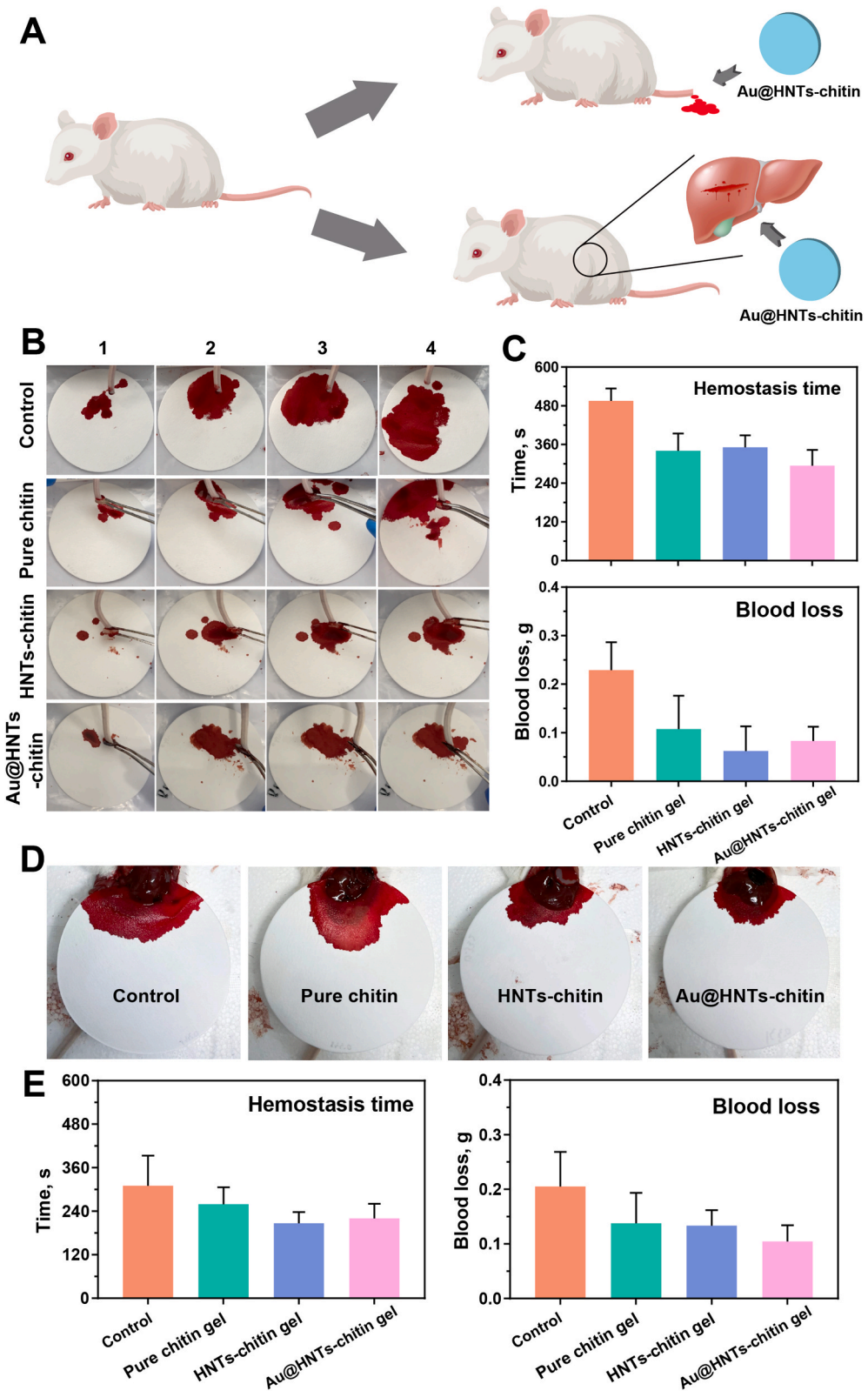

Fig. 7. (A) Schematic representation of the mouse liver and tail hemorrhage model. (B) Photographs of tail hemorrhages in mice at different time periods. (C) Histogram of tail hemostasis time and blood loss in different groups of mice. (D) Photograph of a mouse liver with hemorrhage at the moment when the bleeding finally stopped. (E) Histogram of hemostasis time and blood loss in the liver of mice in different groups.

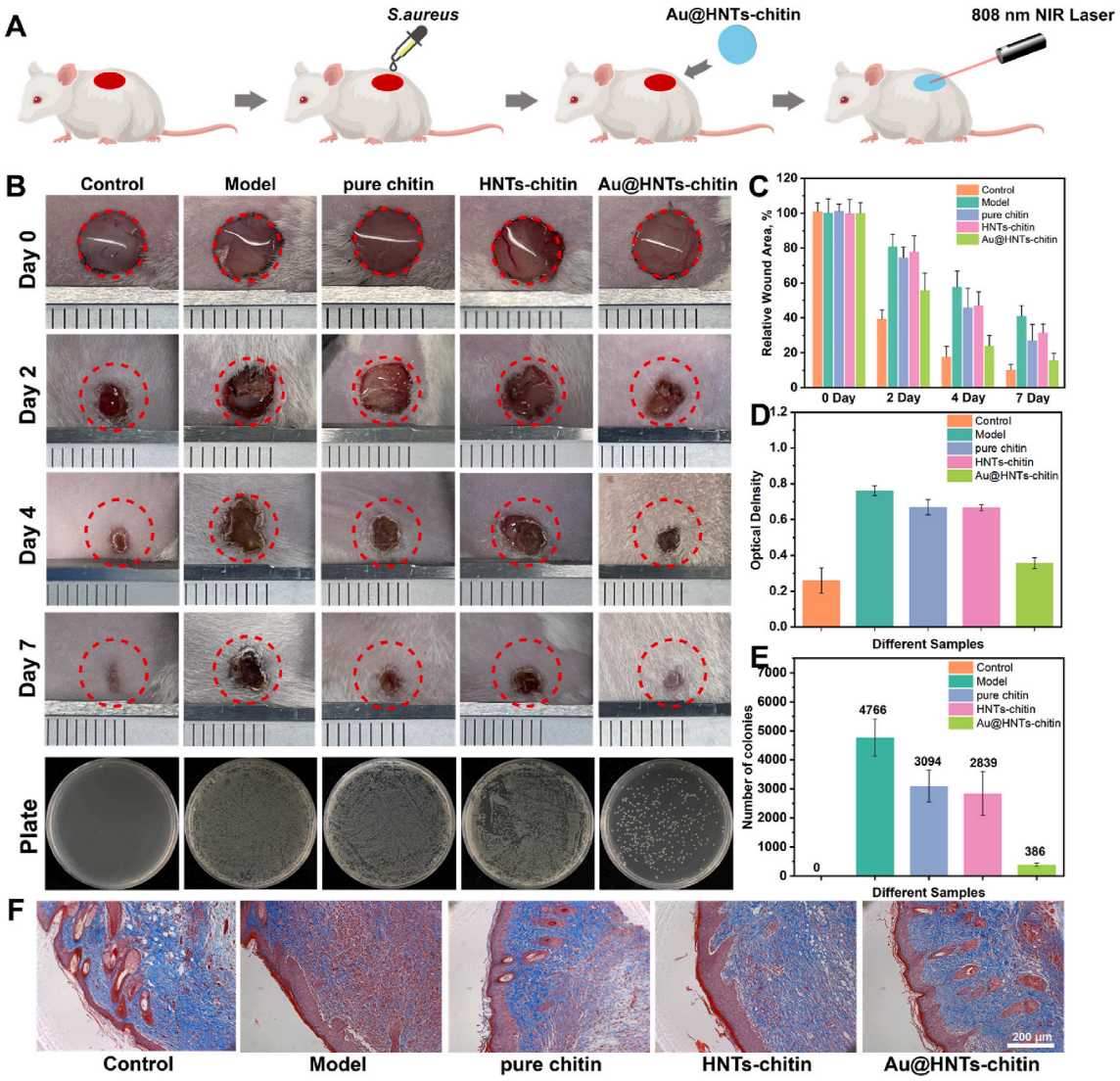

Fig. 8. (A) Operation flow chart of mouse wound healing experiment. (B) Photos of wounds infected for different days in different experimental groups and a photo of colonies of *S. aureus* at the infected site after 12 h of incubation on agar plates. (C) Statistical chart of relative wound area in mice. (D) OD value of bacteria in mouse tissue fluid. (E) Number of colonies on agar plates after 12 h incubation of bacteria in tissue fluid. (F) Tissue Masson staining of mouse wounds on day 7 post-infection.

4. Experimental section

4.1. Materials

Purified HNTs were obtained from Guangzhou Runwo Materials Technology Co., Ltd., China. Chitin (practical grade) was obtained from Shanghai Aladdin Bio-Chem Technology Co., Ltd. $HAuCl_4{\cdot}3H_2O$ was obtained from Shanghai Acmec Biochemical Co., Ltd. OAc (99.8%) and OAm (80–90%) were obtained from Shanghai Aladdin Bio-Chem Technology Co., Ltd. Toluene (99.8%) and ethanol (99.7%, anhydrous) were purchased from Tianjin Yongda Chemical Reagent Co., Ltd., Tianjin, China. Ascorbic acid (99.7%) was purchased from Sinopharm Chemical Reagent Co., Ltd., Shanghai, China. Chitin was obtained from Shanghai Aladdin Bio-Chem Technology Co., Ltd. ECH was acquired by Tianjin Fusheng chemical reagent factory, China. The L929 cell line was purchased from the American Type Culture Collection (USA). All cell culture reagents were ordered from Thermo Fisher Scientific (USA). Acridine orange/Ethidium bromide (AO/EB) staining solution was purchased from Beijing Solarbio Science & Technology Co., Ltd., China. Cell Counting Kit-8 (CCK-8) reagents were acquired from Dojindo Laboratories (Japan). *Escherichia coli* and *Staphylococcus aureus* were obtained from Warner Biotechnology Co., Ltd. Wuhan, China. Ultrapure water was prepared using a Milli-Q Integral Water Purification System (Germany). The animals were ordered from the Guangdong Huawei Testing Co., Ltd., China.

4.2. Preparation of Au@HNTs nanocomposites

Au@HNTs were prepared according to the reported method [27]. Purification of HNTs was performed to remove impurities prior to use [45]. HNTs (15 mg), $HAuCl_4{\cdot}3H_2O$ (22 mg), ethanol (2 mL), toluene (2 mL), oleic acid (0.5 mL), and oleylamine (0.5 mL) were mixed in a beaker and sonicated for 1 min. The mixture was heated to 55 °C under stirring. Then, 10 mg of ascorbic acid was added to the mixture and stirring was continued for 2 min, and the solution turned purple-black, indicating that Au NPs were formed. The obtained Au@HNTs dispersion was centrifuged at 5000 rpm. To isolate free Au NPs, the precipitate was dispersed in toluene by ultrasonication, further centrifuged (4000 rpm, 3 min), and then the supernatant was removed, and the suspension was repeated three times to obtain Au@HNTs. Then, it was dispersed in an ethanol solution, centrifuged at 5000 rpm for 3 min, and the supernatant was discarded to remove toluene. This operation was repeated

three times.

4.3. Preparation of Au@HNTs-chitin and other chitin hydrogels

20 g NaOH and 4 g urea was dissolved in 72 g distilled water. Then 4 g purified chitin powder was dispersed into 98 g NaOH/urea aqueous solution with stirring to obtain a suspension. Subsequently, the suspension was frozen in a cold trap (−75 °C) for 4 h, thawed at room temperature with vigorous stirring. The freezing/thawing cycle was repeated twice to obtain a transparent chitin solution after centrifugation. Then 40 mg HNTs and 40 mg, 20 mg, 10 mg, 0 mg Au@HNTs were added to 10 g the above solution respectively. After stirring for 12 h, epichlorohydrin (ECH) of 0.16 mL as cross-linker was added into the solution. Chitin solution was transferred into a dish, which was placed at 60 °C for 24 h to form a gel, then immerging the gel in 75% ethanol for 12 h. Finally, the obtained chitin hydrogels were washed used water for 3 days, named as HNTs-chitin, 10% Au@HNTs-chitin, 5% Au@HNTs-chitin, 2.5% Au@HNTs-chitin and pure chitin respectively.

4.4. Characterization of Au@HNTs

An aqueous dispersion of HNTs and Au@HNTs (concentration of 0.05%) was dropped onto a copper network with a carbon support film and observed using a transmission electron microscope (JEM-1400Flash, JEOL, Japan) at an accelerating voltage of 120 kV. The UV–vis spectra of all samples were measured by a UV–visible spectrophotometer (UV-2550, Shimadzu Instrument Ltd., Suzhou, China). The XRD analysis was performed using MiniFlex-600, Rigaku Corporation, Japan. The FTIR analysis was performed using Nicolet iS50, Thermo Fisher Scientific Ltd., USA. Dispersion of Au@HNTs and HNTs into poly (sodium-p-styrene sulfonate) solution for particle size and potential measurements. The particle size distribution and ζ potential were obtained using a nano ZS ζ-potential analyzer (Malvern Instruments Co., U. K.). XPS was tested by ESCALAB250Xi, Thermo Fisher Scientific Ltd., USA.

4.5. Catalytic performance evaluation of Au@HNTs

The reduction of 4-NP to 4-AP by $NaBH_4$ was chosen as a model reaction for testing and comparing the catalytic efficiency with pure Au NPs. Typically, 0.15 mL of 4-NP aqueous solution (0.01 m) and catalysts (Au@HNTs 6 mg or pure Au NPs 2 mg or nothing, based on the same Au content) were added into 10 mL deionized water. Subsequently, an aqueous solution of $NaBH_4$ (1.0 mL, 0.1 m) was introduced to the above system. As can be detected by naked-eyes, initial bright yellow solution gradually faded away as the reaction progressed. The absorbance spectra with the maximum peak at 400 nm were used to monitor the reaction progress.

4.6. Characterization of Au@HNT-chitin

The freeze-dried Au@HNTs-chitin hydrogels were sectioned and were sputter coated with 10 nm thick gold-palladium layer and then they were observed with a scanning electron microscope (SEM, Quanta400FEG, FEI, USA). Compression testing of Au@HNTs-chitin was carried out using Zwick/Roell Z005 machine under 25 °C. The samples for compression testing were cylinder samples with diameter of 10 mm and thickness of 1.5 mm. Tests were conducted with a constant strain rate of 2 mm/min and up to 80%. A rotated rheometer (Discovery HR-20, TA Instruments, USA.) was used to measure the dynamic viscosity of Au@HNTs-chitin at the room temperature with the shear rate of 0.1–100 s^{-1}. XRD and FTIR were tested in the same way as Au@HNTs above.

4.7. Photothermal performance of Au@HNT-chitin

To evaluate the photothermal performance of Au@HNTs-chitin, 30 mg Au@HNTs-chitin was placed under the 808 nm laser at 0.8, 1.6, and 2.2 W/cm^2 laser irradiation for 8 min. Once the irradiation started, the temperature of the dispersion was recorded with an infrared camera every 60 s while taking an infrared photograph every 2 min. Each sample was repeated three times to calculate the mean and standard error. Infrared imaging and temperature elevation recordings were monitored using a photothermal imaging system (TiS 55, Fluke Electronic Instrument Ltd., USA). An 808 nm fiber-coupled laser was used (MD–III–808, Changchun New Industry Optoelectronic Technology Ltd., China).

4.8. Cytotoxicity and LIVE/DEAD staining assays

Cytotoxicity evaluation was performed using the Cell Counting Kit 8 (CCK-8) assay. L929 cells (3×10^4 cells/mL) were seeded (100 μL/well) in a 96-well plate. The dishes were pre-incubated overnight in a humidified incubator to obtain cell adhesion. Cell-free medium was used as a blank control. Cells were treated with 0, 7.5, 15, 30 mg/mL and other concentrations, respectively. 0 mg/mL was used as control. After 24 or 48 h of treatment, 10 μL of CCK-8 solution was added to each well for 3 h. Then, the plate was gently mixed for 1 min on an orbital shaker to ensure even distribution of color. Next, absorbance at 450 nm was measured with a microplate reader (Bio-Tek, Hercules, USA). Each experiment was performed three times. The percentage of cell viability was calculated by the following equation:

$$\text{Cell Viability} = \frac{OD_T - OD_0}{OD_C - OD_0} \times 100\%$$

where OD_0 is the value of the blank control, OD_C is the value of the 0 mg/mL control group, OD_T is the value of the test group.

Morphological evidences of death/live cells were analyzed using acridine orange/ethidium bromide (AO/EB) staining. AO was permeable to both dead and live cells, whereas EB can penetrate into dead cells and combines with their DNA and RNA. Hence, the live cells will appear green and dead cells become yellow or orange. L929 cells were inoculated (3×10^4 cells/mL, 1 mL/well) in a 24-well plate and treated with 0, 7.5, 15, 30 mg/mL hydrogel leachate of different samples. An amount of 0 mg/mL was the control. After incubated at 37 °C in 5% CO_2 for 24 or 48 h, the culture supernatants were removed and washed twice with PBS. AO (100 μg/mL), EB (100 μg/mL) and PBS buffer were mixed at a ratio of 1:1:100. Added 500 μL staining solution each well and incubated for 10 min at room temperature without light. The staining solution was removed and used 100 μL of PBS for madefaction. Cells were visualized under a fluorescence microscope (XDY-2, Guangzhou Liss Optical Instrument Ltd., China), and images were taken in random fields.

4.9. Flow cytometry of Annexin V-FITC/PI assay

Two milliliters of L929 cells (3×10^4 cells/mL) were inoculated into 6-well plates overnight for cell adherence and treated with 0, 7.5, 15 and 30 mg/mL hydrogel leachate of different samples. After cultured in an air-humidified incubator for 24 or 48 h, cells were washed with PBS and gently digested by EDTA-free trypsin (0.25%). Collected cells at 800 g for 5 min were centrifuged and suspended in 400 μL of binding buffer. FITC conjugated Annexin-V and propidium iodide (PI) (respectively, 5 μL of each tube) were used to distinguish cells in different apoptosis cycles [46]. After incubated for 10 min at room temperature without light, 1×10^5 stained cells were analyzed using a BD FACSCanto II flow cytometer (BD Biosciences, USA). Fluorescence was detected with the following bandpass filters: 530 nm for Annexin-V-FITC and 670 nm for PI. The results were analyzed by the FlowJo 10.0.2 (BD Biosciences, USA).

4.10. In vitro antibacterial assay of Au@HNTs-chitin

The antibacterial performance of pure chitin, HNTs-chitin and different concentrations of Au@HNTs-chitin was examined through spread plate count method. *Staphylococcus aureus* and *Escherichia coli* (*S. aureus* and *E. coli*) were employed for the antibacterial activity assay. First, 250 μL of the bacterial suspension (1×10^6 CFU/mL) was co-incubated with 30 mg of different hydrogel samples under NIR laser irradiation (808 nm, 1.6 W/cm^2) for 5 min. Then 100 μL of the resulting bacterial suspension was evenly spread on LB agar plates. After 12 h incubation at 37 °C, the plates were photographed and the colonies number on the plate were noted.

4.11. In vitro hemostatic activity assay

The hemostatic properties of the Au@HNTs-chitin were evaluated using a mouse liver trauma model and a mouse tail amputation model. For the mouse liver trauma model, female mice (KM, 5–6 weeks) were anesthetized. The liver of the mouse was exposed through an abdominal incision. After carefully removing the tissue fluid surrounding the liver, a pre-weighed filter paper was placed further below the liver. Hepatic hemorrhage was induced with scissors and then immediately overlay different samples (pure chitin/HNTs-chitin/5% Au@HNTs-chitin) with a diameter of 6 mm on the bleeding site. The group without any treatment after liver hemorrhage was the control group. Data on blood loss and time to hemostasis were recorded throughout the hemostasis process.

A similar hemostatic procedure was performed for the mouse tail amputation model. Cut off 50% of the length of the tail and let the blood drip onto the pre-weighed filter paper. Hydrogel sheets with a diameter of 6 mm (pure chitin, HNTs-chitin, 5% Au@HNTs-chitin) were then applied to the bleeding site with gentle pressure, take a photo every 90 s. The group without any treatment served as the control group. Blood loss and time to hemostasis were then monitored.

4.12. In vivo wound healing assay

To construct a mouse wound infection model, the dorsal surface of mice (female, KM, 5–6 weeks) was depilated to create a 6 mm diameter wound, and then mice were randomly divided into 6 groups: Control, Model, pure chitin, HNTs-chitin, Au@HNTs-chitin. All groups were infected with S. aureus (1×10^6 CFU/mL, 100 μL) except for the group of control after anesthesia. Wounds were exposed to 808 nm laser light (1.6 W/cm^2, 5 min) and photographed in different time periods (0, 2, 4, 7 days) to analyze the wound area with Image J. Pictures of these wounds were taken with a digital camera. The weight of each group of mice was weighed and recorded. After 7 days of different treatments, infected tissues were collected and homogenized for bacterial load assessment. To assess the wound healing process and inflammatory response, histological analysis was performed under Masson's trichrome staining.

CRediT authorship contribution statement

Puxiang Zhao: Conceptualization, Methodology, Investigation, Formal analysis, Data curation, Writing – original draft, Writing – review & editing. **Yue Feng:** Investigation, Methodology, Formal analysis, Writing – review & editing. **Youquan Zhou:** Methodology, Formal analysis, Investigation, Resources. **Cuiying Tan:** Methodology, Formal analysis. **Mingxian Liu:** Project administration, Project design, Funding acquisition, Writing – review & editing, Supervision, Project administration.

Declaration of competing interest

The authors declare no competing interests.

Acknowledgements

This work was financially supported by National Natural Science Foundation of China (52073121), Natural Science Foundation of Guangdong Province (2019A1515011509), Science and Technology Planning Project of Guangzhou (202102010117), and the Fundamental Research Funds for the Central Universities (21622406).

Appendix A. Supplementary data

Supplementary data to this article can be found online at https://doi.org/10.1016/j.bioactmat.2022.05.035.

References

[1] R.J. Tetley, M.F. Staddon, D. Heller, A. Hoppe, S. Banerjee, Y. Mao, Tissue fluidity promotes epithelial wound healing, Nat. Phys. 15 (2019) 1195–1203.
[2] S. Mahmoudi, E. Mancini, L. Xu, A. Moore, F. Jahanbani, K. Hebestreit, R. Srinivasan, X. Li, K. Devarajan, L. Prélot, Heterogeneity in old fibroblasts is linked to variability in reprogramming and wound healing, Nature 574 (2019) 553–558.
[3] J.G. McManus, B.J. Eastridge, C.E. Wade, J.B. Holcomb, Hemorrhage control research on today's battlefield: lessons applied, J. Trauma. Acute Care Surg. 62 (2007) S14.
[4] C. Mao, Y. Xiang, X. Liu, Z. Cui, X. Yang, K.W.K. Yeung, H. Pan, X. Wang, P.K. Chu, S. Wu, Photo-inspired antibacterial activity and wound healing acceleration by hydrogel embedded with Ag/Ag@AgCl/ZnO nanostructures, ACS Nano 11 (2017) 9010–9021.
[5] L.-j. Zhang, C.F. Guerrero-Juarez, T. Hata, S.P. Bapat, R. Ramos, M.V. Plikus, R. L. Gallo, Dermal adipocytes protect against invasive Staphylococcus aureus skin infection, Science 347 (2015) 67–71.
[6] S. Pourshahrestani, E. Zeimaran, I. Djordjevic, N.A. Kadri, M.R. Towler, Inorganic hemostats: the state-of-the-art and recent advances, Mater. Sci. Eng. C 58 (2016) 1255–1268.
[7] J. Margolis, The kaolin clotting time: a rapid one-stage method for diagnosis of coagulation defects, J. Clin. Pathol. 11 (1958) 406.
[8] M. Liu, R. Fakhrullin, A. Novikov, A. Panchal, Y. Lvov, Tubule nanoclay-organic heterostructures for biomedical applications, Macromol. Biosci. 19 (2019), 1800419.
[9] O.P. Setter, E. Segal, Halloysite nanotubes–the nano-bio interface, Nanoscale 12 (2020) 23444–23460.
[10] Y. Feng, X. Luo, F. Wu, H. Liu, E. Liang, R.-R. He, M. Liu, Systematic studies on blood coagulation mechanisms of halloysite nanotubes-coated PET dressing as superior topical hemostatic agent, Chem. Eng. J. 428 (2022), 132049.
[11] X. Zhao, C. Zhou, M. Liu, Self-assembled structures of halloysite nanotubes: towards the development of high-performance biomedical materials, J. Phys. Chem. B 8 (2020) 838–851.
[12] D. Peixoto, I. Pereira, M. Pereira-Silva, F. Veiga, M.R. Hamblin, Y. Lvov, M. Liu, A. C. Paiva-Santos, Emerging role of nanoclays in cancer research, diagnosis, and therapy, Coord. Chem. Rev. 440 (2021), 213956.
[13] P. Zheng, Y. Du, X. Ma, Selective fabrication of iron oxide particles in halloysite lumen, Mater. Chem. Phys. 151 (2015) 14–17.
[14] D.G. Shchukin, G.B. Sukhorukov, R.R. Price, Y.M. Lvov, Halloysite nanotubes as biomimetic nanoreactors, Small 1 (2005) 510–513.
[15] A. Glotov, A. Vutolkina, A. Pimerzin, V. Vinokurov, Y. Lvov, Clay nanotube-metal core/shell catalysts for hydroprocesses, Chem. Soc. Rev. 50 (2021) 9240–9277.
[16] V.A. Vinokurov, A.V. Stavitskaya, Y.A. Chudakov, A.P. Glotov, E.V. Ivanov, P. A. Gushchin, Y.M. Lvov, A.L. Maximov, A.V. Muradov, E.A. Karakhanov, Core-shell nanoarchitecture: schiff-base assisted synthesis of ruthenium in clay nanotubes, Pure Appl. Chem. 90 (2018) 825–832.
[17] C. Anderson, R. Roberts, A comparison of the effects of temperature on wound healing in a tropical and a temperate teleost, J. Fish. Biol. 7 (1975) 173–182.
[18] M. Wigginton, Effects of temperature, oxygen tension and relative humidity on the wound-healing process in the potato tuber, Potato Res. 17 (1974) 200–214.
[19] Y. Cui, Z. Huang, L. Lei, Q. Li, J. Jiang, Q. Zeng, A. Tang, H. Yang, Y. Zhang, Robust hemostatic bandages based on nanoclay electrospun membranes, Nat. Commun. 12 (2021) 1–11.
[20] E.A. Kamoun, E.-R.S. Kenawy, X. Chen, A review on polymeric hydrogel membranes for wound dressing applications: PVA-based hydrogel dressings, J. Adv. Res. 8 (2017) 217–233.
[21] F. Lim, A.M. Sun, Microencapsulated islets as bioartificial endocrine pancreas, Science 210 (1980) 908–910.
[22] H.T. Peng, Hemostatic agents for prehospital hemorrhage control: a narrative review, Mil. Med. Res. 7 (2020) 1–18.
[23] Y. Su, T. Feng, W. Feng, Y. Pei, Z. Li, J. Huo, C. Xie, X. Qu, P. Li, W. Huang Mussel-Inspired, Surface-attachable initiator for grafting of antimicrobial and antifouling hydrogels, Macromol. Rapid Commun. 40 (2019), 1900268.
[24] D.H. Bartlett, F. Azam, Chitin, cholera, and competence, Science 310 (2005) 1775–1777.
[25] B. Duan, Y. Huang, A. Lu, L. Zhang, Recent advances in chitin based materials constructed via physical methods, Prog. Polym. Sci. 82 (2018) 1–33.

[26] J. Huang, Y. Zhong, L. Zhang, J. Cai, Extremely strong and transparent chitin films: a high-efficiency, energy-saving, and "Green" route using an aqueous KOH/Urea solution, Adv. Funct. Mater. 27 (2017), 1701100.
[27] T. Rostamzadeh, M.S. Islam Khan, K. Riche', Y.M. Lvov, A.V. Stavitskaya, J. B. Wiley, Rapid and controlled in situ growth of noble metal nanostructures within halloysite clay nanotubes, Langmuir 33 (2017) 13051–13059.
[28] A. Stavitskaya, K. Mazurova, M. Kotelev, O. Eliseev, P. Gushchin, A. Glotov, R. Kazantsev, V. Vinokurov, Y. Lvov, Ruthenium-loaded halloysite nanotubes as mesocatalysts for Fischer-Tropsch synthesis, Molecules 25 (2020) 1764.
[29] N.M. Sanchez-Ballester, G.V. Ramesh, T. Tanabe, E. Koudelkova, J. Liu, L. K. Shrestha, Y. Lvov, J.P. Hill, K. Ariga, H. Abe, Activated interiors of clay nanotubes for agglomeration-tolerant automotive exhaust remediation, J. Mater. Chem. 3 (2015) 6614–6619.
[30] W. Zhang, F. Tan, W. Wang, X. Qiu, X. Qiao, J. Chen, Facile, template-free synthesis of silver nanodendrites with high catalytic activity for the reduction of p-nitrophenol, J. Hazard Mater. 217 (2012) 36–42.
[31] Y. Du, H. Chen, R. Chen, N. Xu, Synthesis of p-aminophenol from p-nitrophenol over nano-sized nickel catalysts, Appl. Catal. A-Gen. 277 (2004) 259–264.
[32] S. Tang, S. Vongehr, X. Meng, Carbon spheres with controllable silver nanoparticle doping, J. Phys. Chem. C 114 (2010) 977–982.
[33] B. Mu, W. Zhang, A. Wang, Facile fabrication of superparamagnetic coaxial gold/halloysite nanotubes/Fe_3O_4 nanocomposites with excellent catalytic property for 4-nitrophenol reduction, J. Mat. Sci. 49 (2014) 7181–7191.
[34] R. Yan, Y. Zhao, H. Yang, X.J. Kang, C. Wang, L.L. Wen, Z.D. Lu, Ultrasmall Au nanoparticles embedded in 2D mixed-ligand metal–organic framework nanosheets exhibiting highly efficient and size-selective catalysis, Adv. Funct. Mater. 28 (2018), 1802021.
[35] M. Liu, Y. Zhang, J. Li, C. Zhou, Chitin-natural clay nanotubes hybrid hydrogel, Int. J. Biol. Macromol. 58 (2013) 23–30.
[36] K. Feng, G.-Y. Hung, X. Yang, M. Liu, High-strength and physical cross-linked nanocomposite hydrogel with clay nanotubes for strain sensor and dye adsorption application, Compos. Sci. Technol. 181 (2019), 107701.
[37] J.D. Schiffman, C.L. Schauer, Cross-linking chitosan nanofibers, Biomacromolecules 8 (2007) 594–601.
[38] E. Joussein, S. Petit, J. Churchman, B. Theng, D. Righi, B. Delvaux, Halloysite clay minerals—a review, Clay Miner. 40 (2005) 383–426.
[39] N.E. Mushi, J. Kochumalayil, N.T. Cervin, Q. Zhou, L. A. Berglund Nanostructurally, Controlled hydrogel based on small-diameter native chitin nanofibers: preparation, structure, and properties, ChemSusChem 9 (2016) 989–995.
[40] K. Kanimozhi, S.K. Basha, K. Kaviyarasu, V. SuganthaKumari, Salt leaching synthesis, characterization and in vitro cytocompatibility of chitosan/poly (vinyl alcohol)/methylcellulose-ZnO nanocomposites scaffolds using L929 fibroblast cells, J. Nanosci. Nanotechnol. 19 (2019) 4447–4457.
[41] H. Liu, Y. Feng, X. Cao, B. Luo, M. Liu, Chitin nanocrystals as an eco-friendly and strong anisotropic adhesive, ACS Appl. Mater. Interfaces 13 (2021) 11356–11368.
[42] C. Cao, N. Yang, Y. Zhao, D. Yang, Y. Hu, D. Yang, X. Song, W. Wang, X. Dong, Biodegradable hydrogel with thermo-response and hemostatic effect for photothermal enhanced anti-infective therapy, Nano Today 39 (2021), 101165.
[43] H. Zhao, J. Xu, H. Yuan, E. Zhang, N. Dai, Z. Gao, Y. Huang, F. Lv, L. Liu, Q. Gu, 3D printing of artificial skin patches with bioactive and optically active polymer materials for anti-infection and augmenting wound repair, Mater. Horiz. 9 (2022) 342–349.
[44] S. Liu, Q. Zhang, J. Yu, N. Shao, H. Lu, J. Guo, X. Qiu, D. Zhou, Y. Huang, Absorbable thioether grafted hyaluronic acid nanofibrous hydrogel for synergistic modulation of inflammation microenvironment to accelerate chronic diabetic wound healing, Adv. Healthc. Mater. 9 (2020), 2000198.
[45] M. Liu, B. Guo, Q. Zou, M. Du, D. Jia, Interactions between halloysite nanotubes and 2, 5-bis (2-benzoxazolyl) thiophene and their effects on reinforcement of polypropylene/halloysite nanocomposites, Nanotechnology 19 (2008), 205709.
[46] D. Brodoceanu, C. Bauer, E. Kroner, E. Arzt, T. Kraus, Hierarchical bioinspired adhesive surfaces—a review, Bioinspiration Biomimetics 11 (2016), 051001.

Supporting information

Gold@Halloysite Nanotubes-Chitin Composite Hydrogel with Antibacterial and Hemostatic Activity for Wound Healing

Puxiang Zhao[1,2], Yue Feng[1,2], Youquan Zhou[1,2], Cuiying Tan[1,2], Mingxian Liu[1,2]*

[1]Department of Materials Science and Engineering, Jinan University, Guangzhou 510632, China

[2]Engineering Research Center of Artificial Organs and Materials, Ministry of Education, Guangzhou, 510632, PR China

*Corresponding author. Email: liumx@jnu.edu.cn

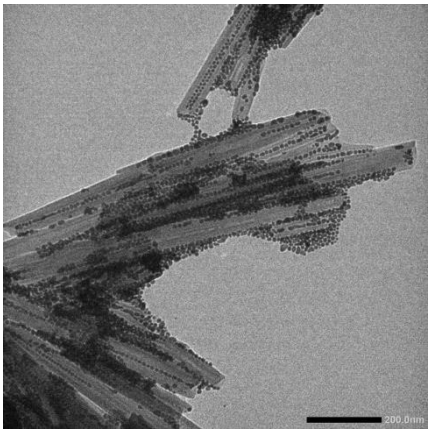

Fig. S1 TEM images of Au@HNTs without centrifugation.

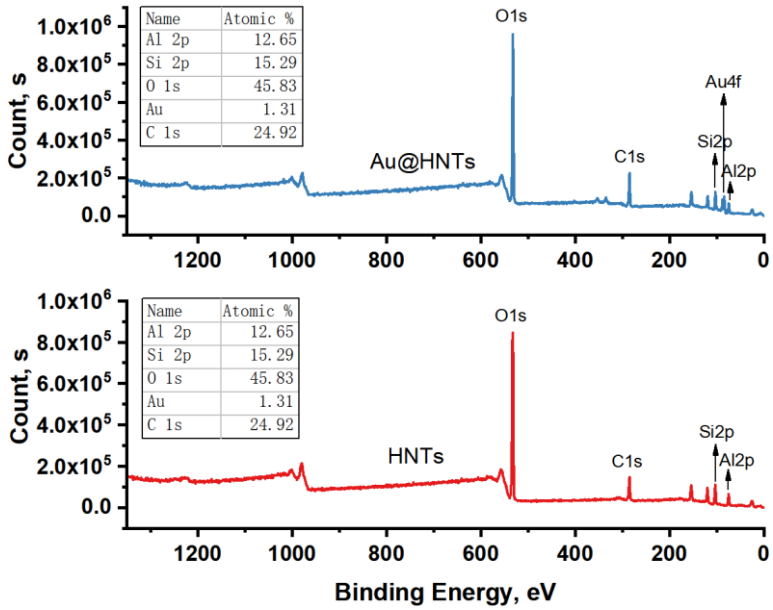

Fig. S2 The survey of XPS spectra of HNTs and Au@HNTs.

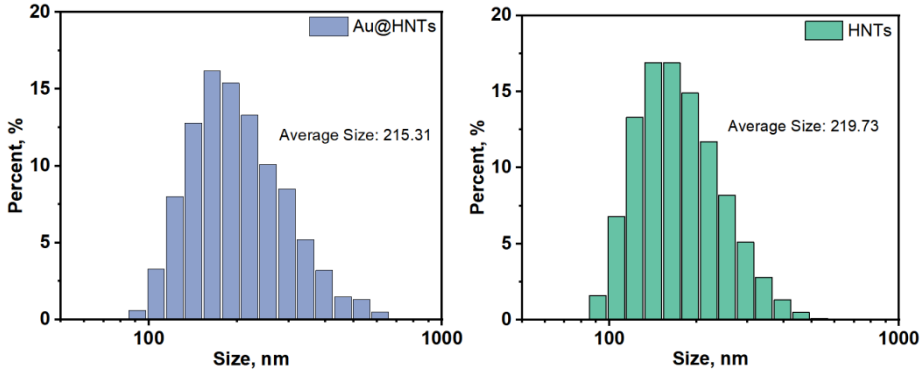

Fig. S3 Particle size distribution of Au@HNTs and HNTs.

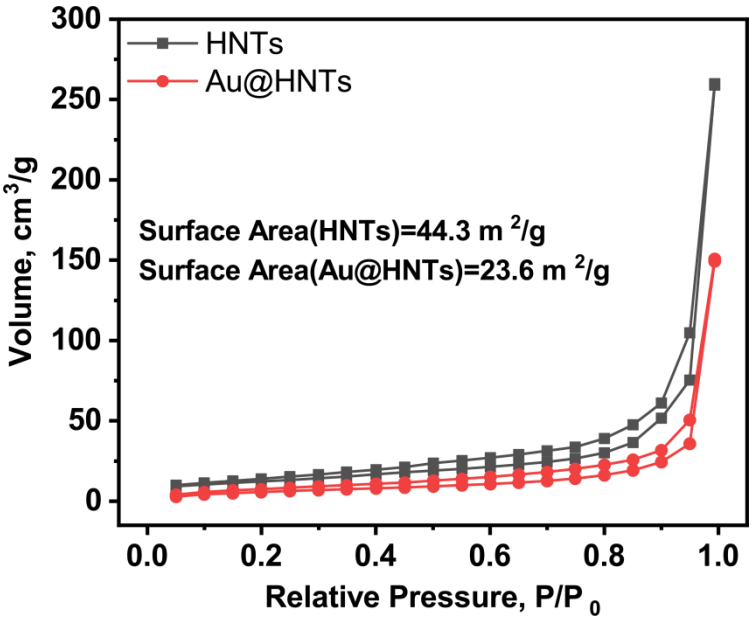

Fig. S4 Nitrogen adsorption rate of Au@HNTs and HNTs.

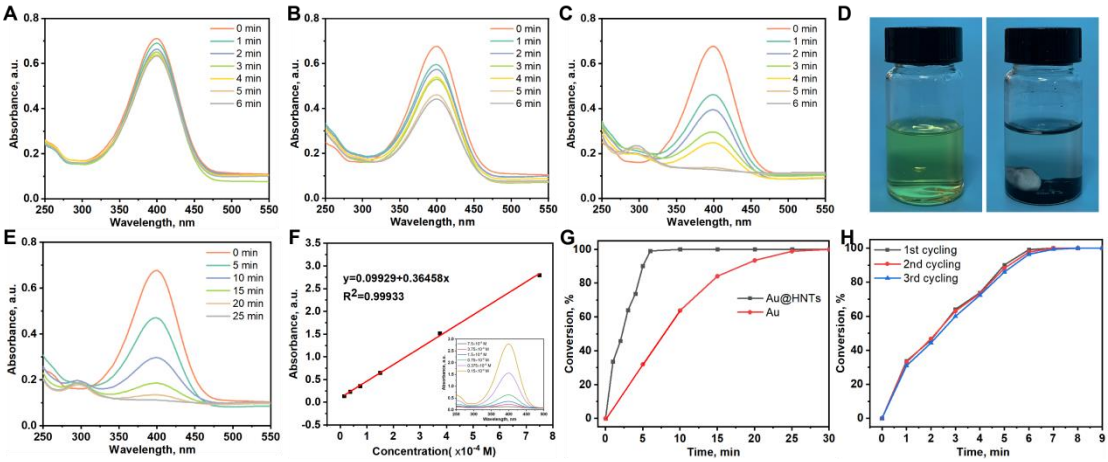

Fig. S5 UV-vis adsorption spectra for the catalytic reduction of 4-NP over no catalyst(A);Au(B) and Au@HNTs(C) in aqueous solution at room temperature in 6 minute. (D) Color change of solution before and after catalysis. (E) UV-vis adsorption spectra for the catalytic reduction of 4-NP over Au in aqueous solution at room temperature in 25 minute. (F) Relationship curve between absorbance and concentration of 4-NP. (G) Catalytic conversion of Au and Au@HNTs. (H) Conversion of Au@HNTs recycled 3 times.

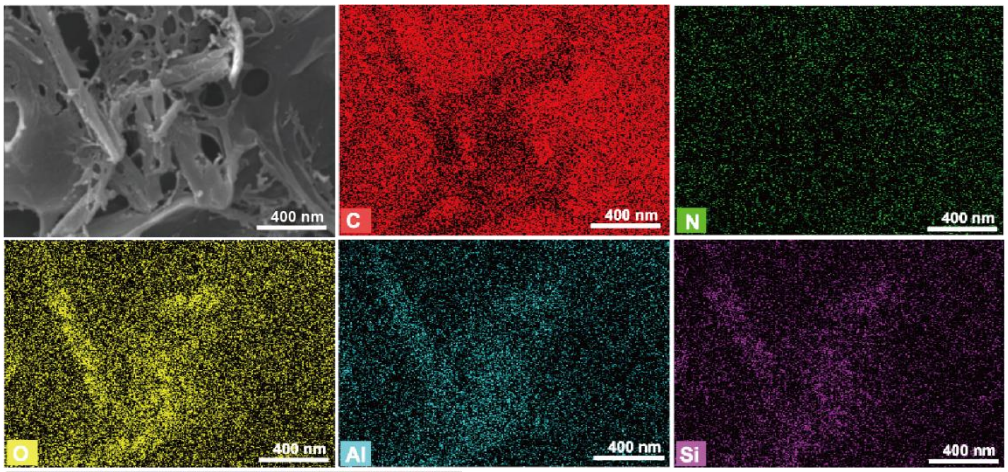

Element	Atomic number	Content(%)
C	6	58.85
N	7	7.88
O	8	25.60
Al	13	2.43
Si	14	5.24

Fig. S6 Mapping images of C, N, O, Al and Si elements of Au@HNTs-chitin.

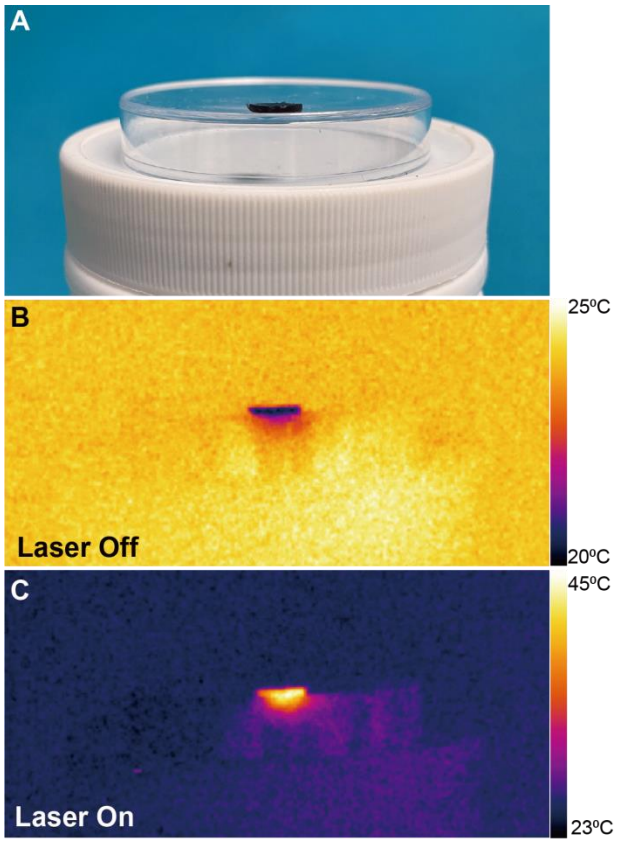

Fig. S7 Appearance (A) and thermal images of the Au@HNTs-chitin hydrogel before (B) and after (C) laser irradiation.

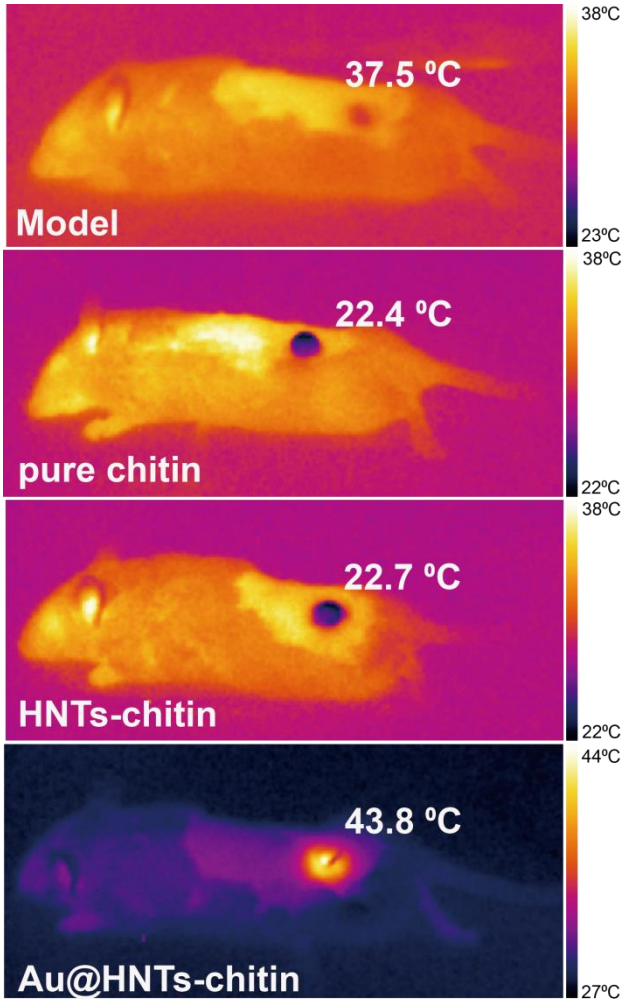

Fig. S8 Thermal images of mice when irradiated with infrared lasers on different hydrogels.

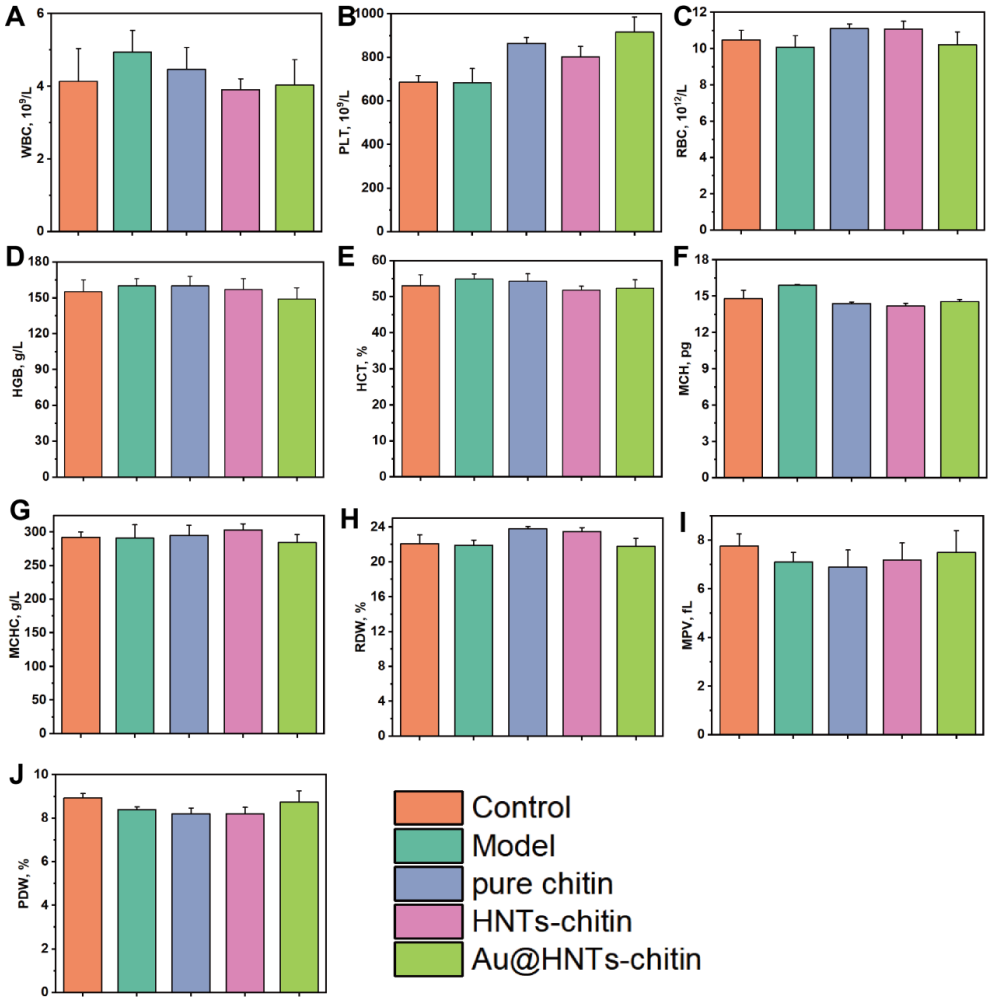

Fig. S9 Blood biochemistry analysis in different treatment groups.

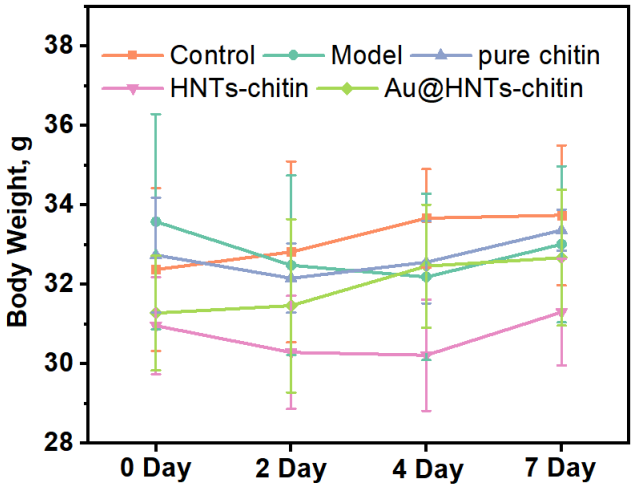

Fig. S10 Changes in body weight of mice after infection at different times.